Obstacle Climbing Improvement of Wheeled Mobile Robots with Extendable Bodies

Saeed Ebrahimi[1], Arman Mardani[2]

[1]*Associate Professor, Department of Mechanical Engineering, Yazd University, Yazd, Iran, ebrahimi@yazd.ac.ir*
[2]*PhD Student, Department of Mechanical Engineering, Yazd University, Yazd, Iran, yovas1369@gmail.com*

ABSTRACT — *As the main objective of this paper, a mechanism-based expanding UGV is proposed to overcome large-scale obstacle. The idea is basically established on scissor mechanism principles which have been innovated in order to achieve long and rigid displacement. Rover platform is composed of the wheels, the main box and a couple of scissor mechanisms adjusting the mass center of rover respect to the wheels. Accordingly, it yields overall control of the contact forces which can simultaneously reduce the slip of the wheels and increase the performance of the obstacle climbing. As the first step, 3D kinematics is derived. Consequently, the stick-slip Euler-Lagrange dynamics is implemented as the dynamic model for a three-level controller and the torque optimization is implemented in order to simulate the rover facing obstacles. Finally, a fixed-geometry rover and the extendable rover are compared with each other to show the enhancement of the climbing ability by using the scissor-based concept. Furthermore, normal contact forces of the wheels are controlled to reduce the slip which consequently, increases the traction force.*

1 Introduction

Today, the space missions and rescue applications obviously required Unmanned Ground Vehicles (UGV)s [1]. Emulation during cold war leaded to the first real application of the UGVs. Consequently, the rover Sojourner [2] was deployed for the Mars Pathfinder lander in July-September 1997. UGVs or autonomous rovers [3, 4] have usually been implemented on the distorted terrains whose coherent and complete survey subject to the surface and environment interaction can be investigated in [5]. Such terrains include hills, holes, and obstacles which may cause horrible fail and halting in the missions of rovers. The four most important issues while interacting unknown terrains are sinkage in the soil [6-9], overturning, failing in obstacle climbing up and continuous slip [10, 11]. Accordingly, unsuccessful climbing up the obstacles is the main issue of the locomotion on the rigid and rough surfaces. While interacting large obstacles, the slip is the most important issue which can cause a broad range of climbing fails [12, 13]. On the other hand, overturning issue can be significantly solved by implementing the stability margins such as ZMP [14]. Regarding each locomotion issue, the contact detection and slip reduction algorithms can be significantly useful in estimating the UGV contact dynamics at each moment and calculating the appropriate actuator torques for reducing the slip [15, 16]. The influence of these algorithms has been investigated for UGVs subject to slip [17]. Furthermore, other methods consider the slip ratio as the base of slip control using high-resolution sensors [18, 19]. Artificial intelligence such as deep learning have been successfully tested to reduce the slip and halting [20]. Notwithstanding the majority of the control-based efforts in this context are conducted to reduce the danger of rover slip when facing medium obstacles, they have not been exploited frequently for large obstacles such as big rocks and walls.

Mechanical reconstruction of UGVs can be advantageous to enhance the climbing performance in passing over large obstacles. The first UGV prototype has been proposed by Walter in 1948 [21] which has inspired other following UGVs such as Tinius in 1950 [5]. Consequently, another diverse designs of UGVs such as Creep Mk-2 in 1962 [22], SAFIR [23], Sojourner [24] and big-wheel-inflatable rovers [25] have been utilized to reduce the danger of slip, halting and increase total traction force. Furthermore, ATHLETE was fabricated to move over large scale obstacles by means of six legs equipped with independent wheels [26]. Despite all ATHLETE adequate abilities, its platform includes expensive limbs and various degrees of freedom besides high power consumption. Accordingly, as a simpler but more efficient designs, high-

mobility UGV, Go-For with wheels-on-legs [27], other fixed-geometry designs [28] and Rhex [29] have been fabricated to eliminate a range of issues. These robots are able to pass some obstacles due to additional legs and limbs. The disadvantages of these platforms are the number of degree of freedom and control issue of the legs.

The proposed extendable UGV in this paper is compounded with a contact-force control algorithm in order to enhance the ability of obstacle climbing and to reduce the danger of slip. The base of the new platform has been found on the scissor mechanism principles. Analogously, in the case of mobile robots, the concept of scissor manipulator is already implemented to handle the camera of the mobile manipulator. As a contribution of the current paper issue, a couple of scissor mechanisms are embedded in the platform which obviously empowers the platform to adjust the distance between the rear wheel, the front wheels, and the main body of the rover. Simultaneously, the controller estimates the normal vector of the surface at the contact point of each wheel using 3D spatial resisting shield sensor [30, 31] and then adjusts scissor length in order to change the contact forces during climbing up. An additional slip reduction algorithm is implemented to eliminate the slip of the wheels during scissor extension by adjusting the torque of the wheels. As it was pointed out previously, the main innovative idea of this paper is to reduce the slip in the presence of large-scale obstacles and distorted surfaces, and enhance the climbing efficiency of the rovers using scissor mechanism.

As the first section, the paper proposes the main idea of the new platform. The second section considers the kinematics of the three wheeled extendable rover. Consequently, 3D stick-slip dynamics of the rover facing large obstacles is extracted. A three-level controller including locomotion control, scissor length control and slip reduction algorithm is used to virtually control the new platform. Finally, the performance of the new rover empowered by the slip reduction algorithm is compared with other fixed-geometry platforms facing obstacles.

2 Concept description

Figure 1-(1, 2, 3) shows the overall form of the new rover. The two scissor mechanisms in Fig. 1-(4), which are constrained by the yellow slot part in Figs. 1-(4,5,6), are the core of the new idea. The variables x_f and x_r (see Figs. 2 and 3) determine the location of the CG with respect to the coordinate system $X_r Y_r Z_r$ for proper distribution of the body weight on the front and rear axles of the robot. It means that the normal forces and consequently, the tractive friction forces of the wheels can be controlled.

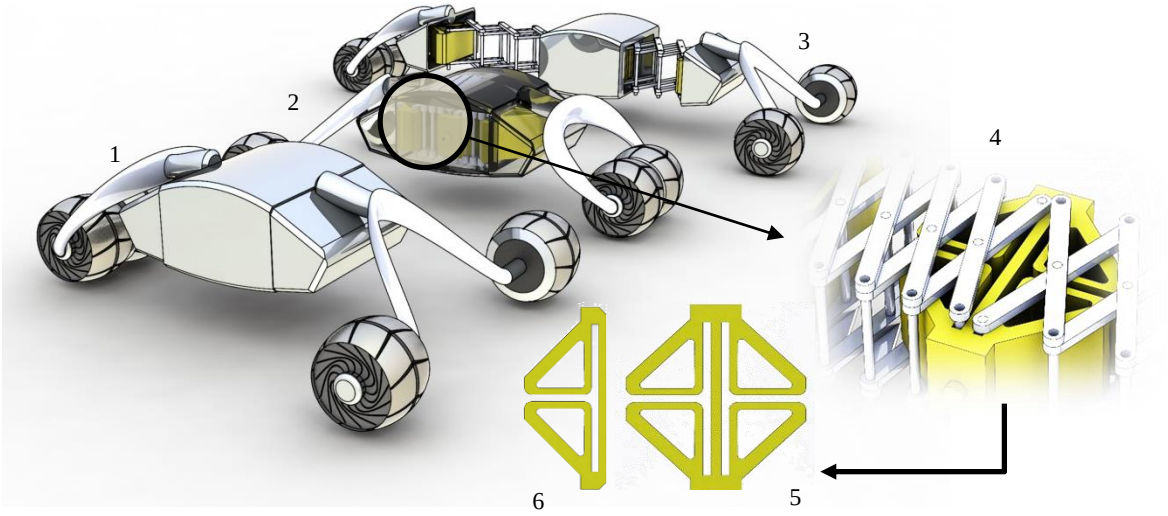

Fig. 1: 1: The new rover, 2: transparent view of the rover, 3: extended rover, 4: slot of scissors, 5: middle slot, 6: side slot

3 Kinematics

The main coordinate systems of the rover model are illustrated in Fig. 2 containing the inertial reference frame XYZ , the coordinate system $X_{CG}^{b} Y_{CG}^{b} Z_{CG}^{b}$ of the CG, and the frames $X_i^{wb} Y_i^{wb} Z_i^{wb}$ $(i = r, fr, fl)$ at the

connection points of the main body and the wheels. Figure 3 represents the geometric dimensions of the rover. For the sake of brevity, all the vectors containing position coordinates and their associated points are respectively written in bold and italic font styles.

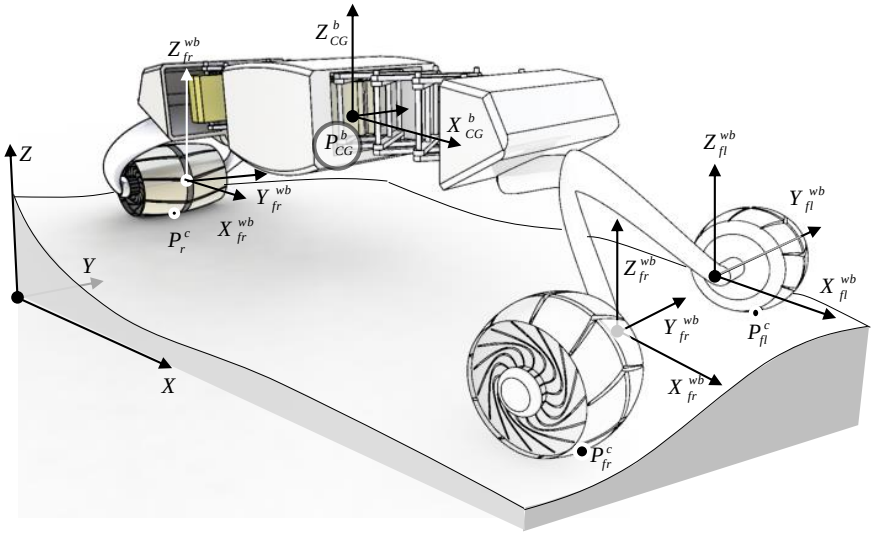

Fig. 2: Coordinate systems of the rover model.

The main body-wheel connection points, the wheel-surface contact points, and the CG point are respectively denoted by $P_i^{wb}\ (i=r,fr,fl), P_i^c$, and $\mathbf{P}_{CG}^b=\begin{bmatrix} x_b & y_b & z_b+H_{CG}^b \end{bmatrix}^{\mathrm{T}}$. The parameters L_b and W_b are the length and the width of the body, respectively. The global orientation of the body is defined using the rotation matrix $\mathbf{R}_b$ representing a rotation of θ_x about the absolute *X* axis, followed by a rotation of θ_y about the absolute *Y* axis, followed by a rotation of θ_z^L about the current Z_{CG}^b axis which can be defined by $\mathbf{R}_b=\mathbf{R}_{Y,\theta_y}\mathbf{R}_{X,\theta_x}\mathbf{R}_{Z_{CG}^b,\theta_z^L}$.

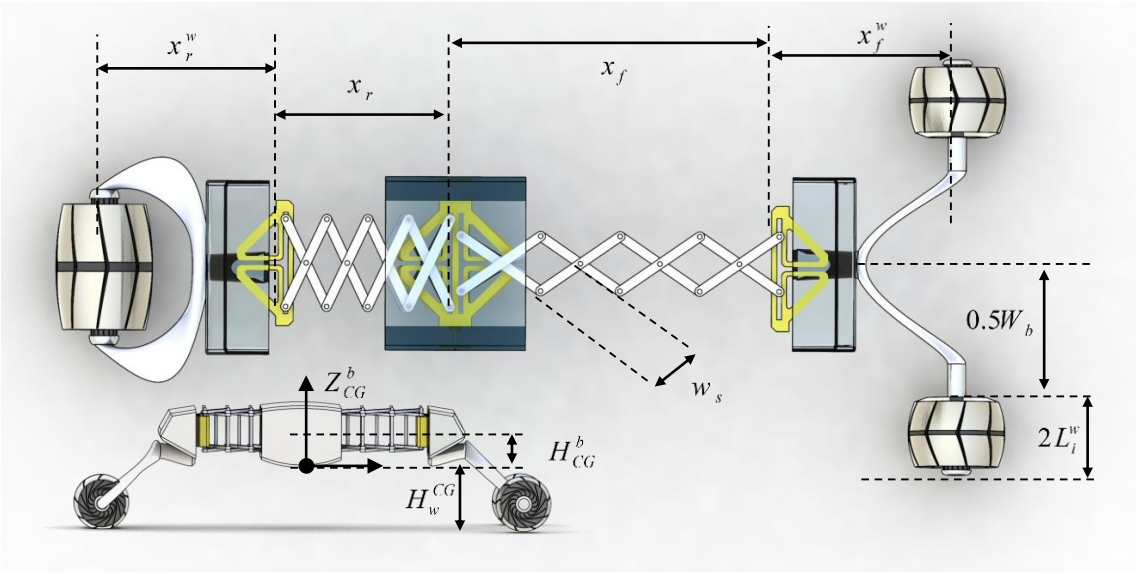

Fig. 3: Dimensions of the platform.

Accordingly, the position coordinates of the main body-wheel connection points can be written as Eq. (1). Figure 4 clearly illustrates the geometric and kinematic parameters of the *i*th wheel.

$$\begin{cases} \mathbf{P}_r^{wb}=\mathbf{R}_b\begin{bmatrix} -x_r-x_r^w & 0 & -H_w^{CG}\end{bmatrix}^{\mathrm{T}}+\mathbf{P}_{CG}^b,\ \mathbf{P}_{fr}^{wb}=\mathbf{R}_b\begin{bmatrix} x_f+x_f^w & -0.5W_b & -H_w^{CG}\end{bmatrix}^{\mathrm{T}}+\mathbf{P}_{CG}^b \\ \mathbf{P}_{fl}^{wb}=\mathbf{R}_b\begin{bmatrix} x_f+x_f^w & 0.5W_b & -H_w^{CG}\end{bmatrix}^{\mathrm{T}}+\mathbf{P}_{CG}^b \end{cases} \quad (1)$$

The parameter $2L_i^w$ denotes the wheel thickness. The point P_i^{cw} denotes the i^{th} wheel center whose coordinates are derived according to Eq. (2).

$$\mathbf{P}_r^{cw} = \mathbf{P}_r^{wb},\ \mathbf{P}_{fr}^{cw} = -L_{fr}^w \mathbf{R}_b \mathbf{e}_y + \mathbf{P}_{fr}^{wb},\ \mathbf{P}_{fl}^{cw} = L_{fl}^w \mathbf{R}_b \mathbf{e}_y + \mathbf{P}_{fl}^{wb} \tag{2}$$

where $[\mathbf{e}_x \quad \mathbf{e}_y \quad \mathbf{e}_z] = \mathbf{I}_{3\times 3}$. To find the absolute coordinates of a point P_i^w on the wheel, its local coordinates with respect to $X_i^{cw} Y_i^{cw} Z_i^{cw}$ have to be derived. As Fig. 4 points out, the plane $P_{ellipse}$ crossing the wheel and passing through its axes results in two ellipses. The diameters of the major and minor axes of each ellipse are denoted as $2L_i^w$ and d_s^o, respectively. Firstly, the body plane P_{body} is defined by axes X_i^w and Z_i^w. The encoder output and the distance between the major axis of the ellipse and the wheel axis are respectively defined by θ_i^n and r_i^β. Consequently, the body plane P_{body} and the angle θ_i^n define the plane $P_{encoder}$ and analogously, $P_{encoder}$ and the angle β_i^n define the plane $P_{ellipse}$. Accordingly, the total angle between the planes P_{body} and $P_{ellipse}$ is equal to ψ_i^n. Independent angle λ_i^n is considered in order to define the parametric equation of the ellipse in its coordinate system $X_i^e Y_i^e Z_i^e$ $(i = r, fr, fl)$. The rotation matrix defining the orientation of the wheel coordinate system $X_i^w Y_i^w Z_i^w$ $(i = r, fr, fl)$ relative to the coordinate system $X_{CG}^b Y_{CG}^b Z_{CG}^b$ of the CG is given by $\mathbf{R}_w^b = \mathbf{R}_{X_i^{wb}, -0.5\pi}$. Consequently, the contact angles ψ_i^n is substituted into the rotation matrix $\mathbf{R}_{ei}^w = \mathbf{R}_{Z_i^w, \psi_i^n} = \mathbf{R}_{Z_i^w, \beta_i^n + \theta_i^n}$ to define the orientation of the coordinate system $X_i^e Y_i^e Z_i^e$ $(i = r, fr, fl)$ relative to the $X_i^w Y_i^w Z_i^w$ $(i = r, fr, fl)$. The coordinates of a typical ellipse point in $X_i^e Y_i^e Z_i^e$ $(i = r, fr, fl)$ are then given by $\mathbf{P}_i^e = 0.5 d_s^o \mathrm{c}_{\lambda_i^n} \mathbf{e}_x + L_i^w \mathrm{s}_{\lambda_i^n} \mathbf{e}_z$ wherein $\mathrm{c}_{(.)}$ and $\mathrm{s}_{(.)}$ denote $\cos(.)$ and $\sin(.)$ respectively. Finally, the coordinates of the point P_i^w can be given by $\mathbf{P}_i^w = \left[\mathbf{R}_b \mathbf{R}_w^b \mathbf{R}_{ei}^w \left(\mathbf{P}_i^e + r_i^\beta \mathbf{e}_x\right)\right] + \mathbf{P}_i^{cw}$.

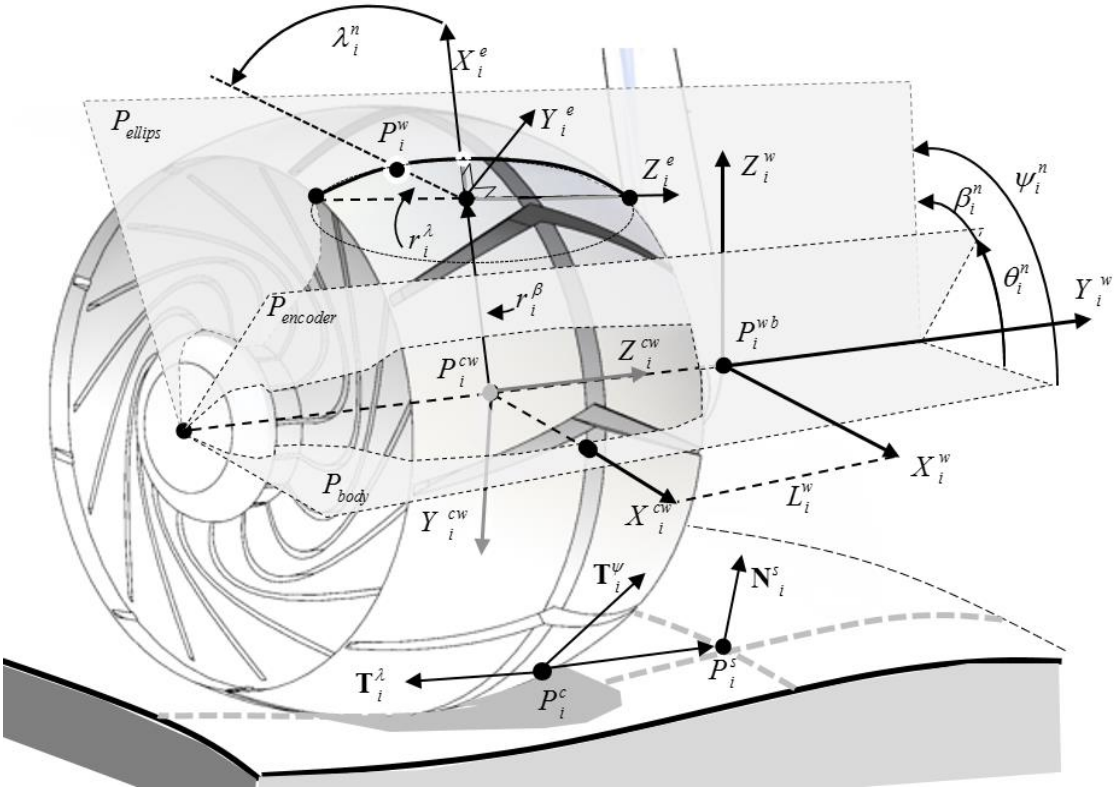

Fig. 4: Kinematic parameters of the i^{th} wheel.

The independent kinematic parameters include the angles θ_x, θ_Y, θ_Z, ψ_i^c, λ_i^c and the coordinates of the point P_{CG}^b. Some of these parameters are determined. The first two coordinates of the point P_{CG}^b, denoted by ${}^x P_{CG}^b$ and ${}^y P_{CG}^b$, specify the desired path in the XY plane of the coordinate system XYZ. The angle θ_Z will be derived in Section 5. The remainder parameters collected in the vector $\mathbf{U}=\left[\theta_x \;\; \theta_y \;\; {}^z P_{CG}^b \;\; \psi_r^c \;\; \lambda_r^c \;\; \psi_{fr}^c \;\; \lambda_{fr}^c \;\; \psi_{fl}^c \;\; \lambda_{fl}^c\right]^{\mathrm{T}}$ have to be modified to satisfy the kinematic constraints. Figure 4 shows the coordinates of the contact point P_i^c on the i^{th} wheel and the coordinates $\mathbf{P}_i^s$ of the vertical projection of the point P_i^c onto the surface $S_{(x,y)}$. The tangent vectors on the wheel at P_i^c and the normal vector of the surface at the contact point of the i^{th} wheel are respectively given by $\mathbf{T}_i^{\lambda}=\partial\Phi/\partial\lambda_i^c$, $\mathbf{T}_i^{\psi}=\partial\Phi/\partial\psi_i^c$ and $\mathbf{N}_i^s=-\partial S_{(x,y)}/\partial x\;\mathbf{e}_x-\partial S_{(x,y)}/\partial y\;\mathbf{e}_y+\mathbf{e}_z$, wherein $\Phi=\mathbf{R}_b\mathbf{R}_w^b\mathbf{R}_{ei}^w\left(\mathbf{P}_i^e+r_i^{\beta}\mathbf{e}_x\right)$. The first set of the kinematic constraints is the tangency condition in which the vector $\mathbf{N}_i^s$ has to be perpendicular to the both vectors $\mathbf{T}_i^{\lambda}$ and $\mathbf{T}_i^{\psi}$ when the i^{th} wheel lies on the surface at the point P_i^c. These constraints are $C_i^{t\lambda}=\mathbf{N}_i^s.\mathbf{T}_i^{\lambda}$ and $C_i^{t\psi}=\mathbf{N}_i^s.\mathbf{T}_i^{\psi}$. Moreover, the distance constraint defines the distance between P_i^c and P_i^s. The first and the second components of $\mathbf{P}_i^c$ are equal to the first and the second components of $\mathbf{P}_i^s$. Accordingly, the distance between the points P_i^s and P_i^c is equal to the difference between the third component of them. The wheel and the surface touch each other by implementing the iterative Newton-Raphson algorithm which reduces the distance between the points P_i^s and P_i^c by imposing the distance constraints $C_i^D=\left|\mathbf{e}_x{}^{\mathrm{T}}\mathbf{P}_i^c-S_{({}^x P_i^c,\,{}^y P_i^c)}\right|$. Simultaneously, it keeps the wheel tangent to the surface according to the tangency constraints. Finally, these constraints are collected in the vector $\mathbf{C}=\left[C_r^{t\lambda}\;C_{fr}^{t\lambda}\;C_{fl}^{t\lambda}\;C_r^{t\psi}\;C_{fr}^{t\psi}\;C_{fl}^{t\psi}\;C_r^D\;C_{fr}^D\;C_{fl}^D\right]^{\mathrm{T}}$ to include all the required kinematic constraints. Implementing the Newton-Raphson algorithm, the coordinates $\mathbf{P}_i^c$ approach to the coordinates $\mathbf{P}_i^s$ and finally, these points touch each other.

4 Stick-Slip Dynamics

In this section, the Lagrange method is implemented to derive the 3D slip-stick dynamics. The independent dynamic parameters are the position and orientation of the CG collected in the vector $\mathbf{P}_b^t=\left[x_b \;\; y_b \;\; z_b \;\; \theta_x \;\; \theta_y \;\; \theta_z^L\right]^{\mathrm{T}}$ and the relative orientations of the wheels which are the encoder data expressed by $\left[\theta_{fl}^e \;\; \theta_{fr}^e \;\; \theta_r^e\right]$. Indeed, the Newton-Raphson algorithm iteratively updates the parameters $\mathbf{U}=\left[\theta_x \;\; \theta_y \;\; {}^z P_{CG}^b \;\; \psi_r^c \;\; \lambda_r^c \;\; \psi_{fr}^c \;\; \lambda_{fr}^c \;\; \psi_{fl}^c \;\; \lambda_{fl}^c\right]^{\mathrm{T}}$ while the generalized coordinates of the dynamic formulation include $\mathbf{v}_d=\left[x_b \;\; y_b \;\; z_b \;\; \theta_x \;\; \theta_y \;\; \theta_z^L \;\; \theta_{fl}^e \;\; \theta_{fr}^e \;\; \theta_r^e\right]^{\mathrm{T}}$. As the first step, the Jacobian matrices of the linear velocities of the wheels center and the CG can be respectively calculated from

$$\left[{}^v\mathbf{J}_i^{cw}\right]_{ij}=\partial\left[\mathbf{P}_i^{cw}\right]_i/\partial\left[\mathbf{v}_d\right]_j \;\;,(i=fl,fr,r),\;\left[{}^v\mathbf{J}_{CG}\right]_{ij}=\partial\left[\mathbf{P}_{CG}^b\right]_i/\partial\left[\mathbf{v}_d\right]_j \qquad (3)$$

The absolute angular velocity $\left[\dot{\theta}_x^b \;\; \dot{\theta}_y^b \;\; \dot{\theta}_z^b\right]^{\mathrm{T}}$ of the main body in terms of $\mathbf{v}_{\mathrm{d}}$ can be represented by $\mathbf{e}_x\dot{\theta}_x+\mathbf{e}_y\dot{\theta}_y+\mathbf{R}_{Y,\theta_y}\mathbf{R}_{X,\theta_x}\mathbf{e}_z\dot{\theta}_z^L$. Accordingly, the absolute angular velocity of the wheels $\left[\dot{\theta}_x^i \;\; \dot{\theta}_y^i \;\; \dot{\theta}_z^i\right]^{\mathrm{T}}$ can be calculated by $\left[\dot{\theta}_x^b \;\; \dot{\theta}_y^b \;\; \dot{\theta}_z^b\right]^{\mathrm{T}}+\mathbf{R}_b\mathbf{R}_w^b\mathbf{e}_z\dot{\theta}_i^n$. Subsequently, the angular velocity Jacobians can be obtained as

$$
\begin{aligned}
{}^{\omega}\mathbf{J}_{fl}^{cw} &= \begin{bmatrix} \mathbf{O}_{3\times3} & \mathbf{e}_x & \mathbf{e}_y & \mathbf{R}_{Y,\theta_y}\mathbf{R}_{X,\theta_x}\mathbf{e}_z & \mathbf{R}_b\mathbf{R}_w^b\,\mathbf{e}_z & \mathbf{O}_{3\times2} \end{bmatrix}_{3\times9} \\
{}^{\omega}\mathbf{J}_{fr}^{cw} &= \begin{bmatrix} \mathbf{O}_{3\times3} & \mathbf{e}_x & \mathbf{e}_y & \mathbf{R}_{Y,\theta_y}\mathbf{R}_{X,\theta_x}\mathbf{e}_z & \mathbf{O}_{3\times1} & \mathbf{R}_b\mathbf{R}_w^b\,\mathbf{e}_z & \mathbf{O}_{3\times1} \end{bmatrix}_{3\times9} \\
{}^{\omega}\mathbf{J}_{r}^{cw} &= \begin{bmatrix} \mathbf{O}_{3\times3} & \mathbf{e}_x & \mathbf{e}_y & \mathbf{R}_{Y,\theta_y}\mathbf{R}_{X,\theta_x}\mathbf{e}_z & \mathbf{O}_{3\times2} & \mathbf{R}_b\mathbf{R}_w^b\,\mathbf{e}_z \end{bmatrix}_{3\times9} \\
{}^{\omega}\mathbf{J}_{CG} &= \begin{bmatrix} \mathbf{O}_{3\times3} & \mathbf{e}_x & \mathbf{e}_y & \mathbf{R}_{Y,\theta_y}\mathbf{R}_{X,\theta_x}\mathbf{e}_z & \mathbf{O}_{3\times3} \end{bmatrix}_{3\times9}
\end{aligned}
\tag{4}
$$

The augmented total Jacobian matrix of the wheels and body can now be defined by $\mathbf{J}_i^{cw} = \begin{bmatrix} \begin{bmatrix} {}^{v}\mathbf{J}_i^{cw} \end{bmatrix}^{\mathrm{T}} & \begin{bmatrix} {}^{\omega}\mathbf{J}_i^{cw} \end{bmatrix}^{\mathrm{T}} \end{bmatrix}_{6\times9}^{\mathrm{T}}$ and $\mathbf{J}_{CG} = \begin{bmatrix} {}^{v}\mathbf{J}_{CG}^{\mathrm{T}} & {}^{\omega}\mathbf{J}_{CG}^{\mathrm{T}} \end{bmatrix}_{6\times9}^{\mathrm{T}}$, respectively. The mass matrix and the Christoffel index can be written as

$$
\begin{aligned}
\mathbf{D}_{5\times5} &= {}^{v}\mathbf{J}_{CG}^{\mathrm{T}} m_i\, {}^{v}\mathbf{J}_{CG} + {}^{\omega}\mathbf{J}_{CG}^{\mathrm{T}} I_i\, {}^{\omega}\mathbf{J}_{CG} + \sum_{i=(fl,fr,r)} [{}^{v}\mathbf{J}_i^{cw}]^{\mathrm{T}} m_i\, {}^{v}\mathbf{J}_i^{cw} + \begin{bmatrix} {}^{\omega}\mathbf{J}_i^{cw} \end{bmatrix}^{\mathrm{T}} I_i\, {}^{\omega}\mathbf{J}_i^{cw} \\
[\mathbf{C}_{chr}]_{\mathrm{k}} &= \frac{1}{2}\sum_{i=1}^{5}\sum_{j=1}^{5}\left(\partial[\mathbf{D}]_{kj}/\partial[\mathbf{v}_d]_i + \partial[\mathbf{D}]_{ki}/\partial[\mathbf{v}_d]_j - \partial[\mathbf{D}]_{ij}/\partial[\mathbf{v}_d]_k\right)[\dot{\mathbf{v}}_d]_i\,[\dot{\mathbf{v}}_d]_j
\end{aligned}
\tag{5}
$$

The effect of the gravity can be obtained in the following manner

$$
\mathbf{G} = \partial\left(\mathbf{e}_z^{\mathrm{T}} g\,(\mathbf{P}_{CG}^b + \sum_{i=(b,wf,wr)} m_i \mathbf{P}_i^{cw})\right)\Big/\partial v_d \tag{6}
$$

The Jacobean matrix of the contact point $\begin{bmatrix} {}^{v}\mathbf{J}_i^c \end{bmatrix}_{ij}$ is equal to $\partial\begin{bmatrix}\mathbf{P}_i^c\end{bmatrix}/\partial[\mathbf{v}_d]_j$. The rotation matrix defining the orientation of the contact point coordinate system $X_i^{pc}Y_i^{pc}Z_i^{pc}$ relative to the coordinate system XYZ is given by $\mathbf{R}_{pc} = \begin{bmatrix} \mathbf{T}_i^{\lambda} & \mathbf{T}_i^{\psi} & \mathbf{N}_i^{s} \end{bmatrix}$. Representation of the global contact force $\mathbf{F}_i$ of the wheel *i* in the frame $X_i^{pc}Y_i^{pc}Z_i^{pc}$ leads to the local contact force $\mathbf{F}_i^c = \mathbf{R}_{pc}^{\mathrm{T}}\mathbf{F}_i$ whose components are aligned with the directions of $\mathbf{T}_i^{\lambda}$, $\mathbf{T}_i^{\psi}$, and $\mathbf{N}_i^{s}$ vectors. Accordingly, the generalized local contact force can be written as $\mathbf{F}_i^{cp} = \begin{bmatrix} {}^{v}\mathbf{J}_i^c \end{bmatrix}^{\mathrm{T}}\mathbf{F}_i = \begin{bmatrix} {}^{v}\mathbf{J}_i^c \end{bmatrix}^{\mathrm{T}}\mathbf{R}_{pc}\mathbf{F}_i^c$. The dynamic equations of motion can be described as

$$
\mathbf{D}\,\ddot{\mathbf{v}}_d + \mathbf{C}_{chr} + \mathbf{G} + \sum_i \mathbf{F}_i^{cp} = \mathbf{D}\,\ddot{\mathbf{v}}_d + \mathbf{C}_{chr} + \mathbf{G} + \sum_i \begin{bmatrix} {}^{v}\mathbf{J}_i^c \end{bmatrix}^{\mathrm{T}}\mathbf{R}_{pc}\mathbf{F}_i^c = \mathbf{Q} \tag{7}
$$

which can be rearranged in the following form as

$$
\begin{aligned}
&\boldsymbol{\chi}_D\,\boldsymbol{\Theta} = \boldsymbol{\chi}_{\tau},\ \boldsymbol{\chi}_{\tau} = \begin{bmatrix} \mathbf{Q} - (\mathbf{C}_{chr} + \mathbf{G}) \end{bmatrix}_{9\times1} \\
&\boldsymbol{\Theta} = \begin{bmatrix} (\ddot{\mathbf{v}}_d)^{\mathrm{T}} & \mathbf{F}_{fl}^{cp\,\mathrm{T}} & \mathbf{F}_{fr}^{cp\,\mathrm{T}} & \mathbf{F}_{r}^{cp\,\mathrm{T}} \end{bmatrix}_{18\times1}^{\mathrm{T}},\ \boldsymbol{\chi}_D = \begin{bmatrix} \mathbf{D} & \begin{bmatrix} {}^{v}\mathbf{J}_{fl}^c \end{bmatrix}^{\mathrm{T}}\mathbf{R}_{pc} & \begin{bmatrix} {}^{v}\mathbf{J}_{fr}^c \end{bmatrix}^{\mathrm{T}}\mathbf{R}_{pc} & \begin{bmatrix} {}^{v}\mathbf{J}_{r}^c \end{bmatrix}^{\mathrm{T}}\mathbf{R}_{pc} \end{bmatrix}_{9\times18}
\end{aligned}
\tag{8}
$$

The vector $\mathbf{Q}$ represents the external forces and torques. These equations have to be solved in order to obtain the contact forces and the generalized accelerations in terms of the generalized coordinates. Some additional acceleration equations are to be included in the dynamic equations (8) to achieve equal number of equations and unknowns. The representation of the absolute contact point velocity $\dot{\mathbf{P}}_i^c$ in the coordinate system $X_i^{pc}Y_i^{pc}Z_i^{pc}$ leads to $\dot{\mathbf{P}}_i^{pc} = \mathbf{R}_{pc}^{\mathrm{T}}\dot{\mathbf{P}}_i^c$. This velocity can be represented in terms of the generalized coordinates as $\dot{\mathbf{P}}_i^{pc} = \mathbf{R}_{pc}^{\mathrm{T}}\,{}^{v}\mathbf{J}_i^c\dot{\mathbf{v}}_d$. To impose the stick condition for wheel *i*, $\dot{\mathbf{P}}_i^{pc}$ has to be set to zero. Consequently, differentiating $\mathbf{R}_{pc}^{\mathrm{T}}\,{}^{v}\mathbf{J}_i^c\dot{\mathbf{v}}_d$ with respect to time yields the required acceleration equations $\left(\mathbf{R}_{pc}^{\mathrm{T}}\,{}^{v}\mathbf{J}_i^c\right)\ddot{\mathbf{v}}_d = \left(-\partial\left(\mathbf{R}_{pc}^{\mathrm{T}}\,{}^{v}\mathbf{J}_i^c\right)/\partial t\right)\dot{\mathbf{v}}_d$, which upon rearrangement, can be written as

$$\boldsymbol{\chi}_i^p \boldsymbol{\Theta} = \boldsymbol{\chi}_i^{\tau p},\ \boldsymbol{\chi}_i^p = \left[\left(\mathbf{R}_{pc}^{\mathrm{T}}\ {}^{v}\mathbf{J}_i^c \right) \quad \mathbf{O}_{3\times 9} \right]_{3\times 18},\ \boldsymbol{\chi}_i^{\tau} = \left[\left(-\partial \left(\mathbf{R}_{pc}^{\mathrm{T}}\ {}^{v}\mathbf{J}_i^c \right) / \partial t \right) \dot{\mathbf{v}}_d \right]_{3\times 1} \tag{9}$$

By appending Eq. (9) for three wheels to Eq. (8), the system of dynamic equations can now be solved for all unknowns under the stick assumption. The stick assumption may only be violated when the resultant friction force exceeds the maximum allowable static friction according to $\mu_s \mathbf{e}_z^{\mathrm{T}} \mathbf{F}_i^{cp} < \sqrt{\left(\mathbf{e}_x^{\mathrm{T}} \mathbf{F}_i^{cp} \right)^2 + \left(\mathbf{e}_y^{\mathrm{T}} \mathbf{F}_i^{cp} \right)^2}$. This condition means when the contact force vector lies outside the friction cone, the slip occurs. In this case, the unknown contact forces of the wheels along the slip directions in Eq. (8) have to be replaced by the corresponding kinetic friction forces. This, in turn, leads to the reduction of unknown parameters. The kinetic friction force vector in the global and local frames can be defined respectively by $-\mu_k \mathbf{e}_z^{\mathrm{T}} \mathbf{F}_i^{cp}\ \dot{\mathbf{P}}_i^c / \left\| \dot{\mathbf{P}}_i^c \right\|$ and $-\mu_k \mathbf{e}_z^{\mathrm{T}} \mathbf{F}_i^{cp}\ \mathbf{R}_{pc}^{\mathrm{T}} \dot{\mathbf{P}}_i^c / \left\| \dot{\mathbf{P}}_i^c \right\|$. The simulation algorithm checks all possible stick-slip condition to find a consistent solution.

5 Geometric control of scissors length

The geometry of control system is illustrated in Fig. 6. The control process has three main levels including the scissors control to adjust the values of scissors length x_f and x_r, the kinematic control to approach the desired point P_d^{xyz}, and the torque optimization to reduce the slips by implementing dynamic estimation. At the beginning of each simulation step, the controller finds the appropriate scissors length according to the third component of the normal vector at contact points. Consequently, using the new scissors length, the kinematic controller produces the desired velocities of the main body in order to reduce the position error. Finally, implementing the produced velocities from the previous control level, the dynamics estimator unit finds a set of torques for the wheel motors which prevents slip. Due to the influence of the normal vector at the contact point of the wheel i ($\mathbf{N}_i^s$) on the tractive friction force, its magnitude and direction can be assumed as an appropriate measure to find x_i.

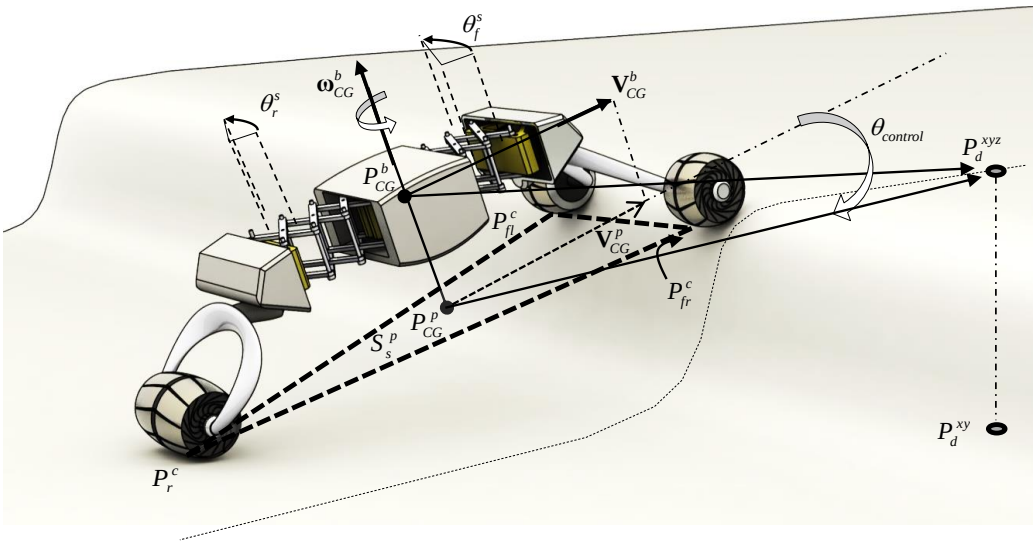

Fig. 5: Geometry of the control system.

Accordingly, the pivot angles θ_f and θ_r in scissors can be changed to achieve the desired x_f and x_r. The gravity force influences both the friction and normal contact forces of the wheels moving on the ramps. Obviously, by increasing the angle of the ramp, the friction becomes dominant and the effect of normal contact forces reduces. Assuming the adjustable center of mass, the values of the normal and friction forces can be controlled. As an example, when the front wheels are located on a ramp and the rear wheel is moving on a flat surface, the scissors length can be adjusted in such a way that the center of mass is approached the rear wheel. This helps the platform to increase the rear normal contact force, and consequently, the possible

tractive friction force of the rear wheel in the stick zone is increased as well. Hence, the concept of this idea can be formulized to relate the desired scissors length to the normal contact forces whereby the influence of the traction force of the wheel on the flat surface is increased. Equation (10) proposes this idea as follows

$$0.5\mathbf{e}_z^{\mathrm{T}}\left(\mathbf{N}_{fl}^{s}+\mathbf{N}_{fr}^{s}\right)x_{fd}-\mathbf{e}_z^{\mathrm{T}}\mathbf{N}_{r}^{s}x_{rd}=0,\quad x_{fd}+x_{rd}=L_t \tag{10}$$

where the constant L_t is a user-defined value equal to the maximum length of one scissor. The current values of x_f and x_r have to approach the desired values x_{fd} and x_{rd} by a PID controller. As the second level of the control process, the spatial kinematics of the robot is controlled by a PID controller in order to find desired angular velocity of the wheels' motor according to the distance between the points P_{CG}^{p} and P_d^{xyz}. According to Fig. 6, the robot can only move along the vector $\mathbf{V}_{CG}^{b}$ as its platform is assumed to be nonholonomic. The robot can also rotate about Z_{CG}^{b} axis. Two control vectors are the velocity vector $\mathbf{V}_{CG}^{b}$ and the angular velocity vector $\boldsymbol{\omega}_{CG}^{b}$ of the main body. The coordinates of the desired and the estimated points are respectively given by $\mathbf{P}_d^{xyz}$ and ${}^{e}\mathbf{P}_{CG}^{b}$. The first and the second coordinates of the point P_d^{xyz} specify a planar point P_d^{xy} whose coordinates are defined by $\mathbf{P}_d^{xy}$. The third coordinate of the point P_d^{xyz} is equal to $S_{(x=[1\ \ 0]\mathbf{P}_d^{xy},\,y=[0\ \ 1]\mathbf{P}_d^{xy})}$. The projection point of the point ${}^{e}P_{CG}^{b}$ onto the plane S_p^s defined by three estimated contact points ${}^{e}P_i^c$ $(i=r,fr,fl)$ is denoted by P_{CG}^{p}. The vector $\mathbf{V}_d^c$ is generated by projecting the vector $\mathbf{P}_d^{xyz}$-$\mathbf{P}_{CG}^{p}$ onto the surface at the point P_{CG}^{p}. Projection of $\mathbf{V}_d^c$ onto the robot plane defined by three points P_r^{cw}, P_{fr}^{cw} and P_{fl}^{cw} is denoted by $\mathbf{V}_d^p$. The angular velocity $\boldsymbol{\omega}_{CG}^{b}$ required for aligning the robot with the vector $\mathbf{V}_d^p$ is derived by $\boldsymbol{\omega}_{CG}^{b}=\left(\mathbf{V}_{CG}^{b}\times\mathbf{V}_d^p\right)\left\|\mathbf{V}_{CG}^{b}\times\mathbf{V}_d^p\right\|^{-1}K_{\omega}$. The parameter K_{ω} is the controller coefficient to define the magnitude of the required rotational velocity. The angle θ_Z can be updated by the equation $\theta_Z\,\boldsymbol{\omega}_{CG}^{b}=\left\|\boldsymbol{\omega}_{CG}^{b}\right\|\int_{t=0}^{t}\boldsymbol{\omega}_{CG}^{b}dt$. The required velocity vector of $\mathbf{V}_{CG}^{b}$ is calculated as $\mathbf{V}_{CG}^{b}={}^{e}\mathbf{R}_b\,\mathbf{e}_x^{\mathrm{T}}\left\|\mathbf{P}_{CG}^{p}-\mathbf{P}_d^{XYZ}\right\|K_v$. The parameter K_v is the control coefficient of $\mathbf{V}_{CG}^{b}$. The vectors $\mathbf{V}_{CG}^{b}$ and $\boldsymbol{\omega}_{CG}^{b}$ have to be used to find the desired encoder velocity $\dot{\theta}_i^d$ (see Fig. 6). The total angular velocity of the i^{th} wheel can be seen in the following equation

$$\left[\dot{\theta}_{X_{CG}^{b}}^{b}\quad\dot{\theta}_{Y_{CG}^{b}}^{b}\quad 0\right]^{\mathrm{T}}+\boldsymbol{\omega}_{CG}^{b}+\mathbf{R}_b\mathbf{R}_w^{b}\mathbf{R}_{oi}^{w}\left[0\quad 0\quad\theta_i^d\right]^{\mathrm{T}}=\left(\mathbf{P}_i^c-\mathbf{P}_i^{cw}\right)\times\dot{\mathbf{P}}_i^{cw}\,\|\,\mathbf{P}_i^c-\mathbf{P}_i^{cw}\,\|^{-2} \tag{11}$$

The desired angular velocity of the wheels' motors as the final output of the controller is given by

$$\dot{\theta}_i^d=\mathbf{e}_z\left(\left[\mathbf{R}_{oi}^{w}\right]^{\mathrm{T}}\left[\mathbf{R}_w^{b}\right]^{\mathrm{T}}\mathbf{R}_b^{\mathrm{T}}\left(\left(\mathbf{P}_i^c-\mathbf{P}_i^{cw}\right)\times\dot{\mathbf{P}}_i^{cw}\,\|\,\mathbf{P}_i^c-\mathbf{P}_i^{cw}\,\|^{-2}-\left[\dot{\theta}_{X_{CG}^{b}}^{b}\quad\dot{\theta}_{Y_{CG}^{b}}^{b}\quad 0\right]^{\mathrm{T}}+\boldsymbol{\omega}_{CG}^{b}\right)\right) \tag{12}$$

6 Optimization of the motor torques of the wheels

Finding the required torques of the motors is the final level of the control process. As the first step, the angular velocity extracted from the kinematic control level restricts the acceptable range of the torque for each wheel. The second step is to optimize the torques in these ranges whereby the rover moves without longitudinal slip. In order to accurately solve the dynamic equations, the contact sensor data including the angles λ_i and β_i is required [31]. For the slip elimination, the motor torques can be obtained and applied during the real time dynamic analysis. For this purpose, a direct search method illustrated in Fig. 7 is implemented to find the optimal torques. The proportional and derivative coefficients respectively denoted by $K_{ai}K_c$ and $K_{ai}D_c$ are implemented in a PD controller whereby the current velocity $\dot{\theta}_i^n$ of the motors approaches to $\dot{\theta}_i^d$. These coefficients are both the result of multiplication of a scale constant K_{aj} and two

different fraction constants K_c and D_c. Choosing two different values of K_{aj} results in two different torques which both of them reduce the control error $\dot{\theta}_i^d - \dot{\theta}_i^n$. Accordingly, an allowable output torque range can be extracted by choosing K_{a1} and K_{a2} as the following equation represents

$$\begin{cases} \tau_{i1} = K_{a1}\left(K_c\left(\dot{\theta}_i^d - \dot{\theta}_i^n\right) + D_c\left(\ddot{\theta}_i^d - \ddot{\theta}_i^n\right)\right), \quad \tau_{i2} = K_{a2}\left(K_c\left(\dot{\theta}_i^d - \dot{\theta}_i^n\right) + D_c\left(\ddot{\theta}_i^d - \ddot{\theta}_i^n\right)\right) \\ \min(\tau_{i1}, \tau_{i2}) \le \tau_i \le \max(\tau_{i1}, \tau_{i2}) \end{cases} \tag{13}$$

The optimization process reducing the slip is illustrated in Fig. 7. The optimization is conducted to find a set of τ_i according to a blind search in the range of $\min(\tau_{i1}, \tau_{i2})$ and $\max(\tau_{i1}, \tau_{i2})$. The cost function $S = \left(\mu_s \mathbf{e}_z^{\mathrm{T}} \mathbf{F}_i^{cp}\right)^{-1} \sqrt{\left(\mathbf{e}_x^{\mathrm{T}} \mathbf{F}_i^{cp}\right)^2 + \left(\mathbf{e}_y^{\mathrm{T}} \mathbf{F}_i^{cp}\right)^2}$ used in the algorithm defines the danger of slip and is presented as a fraction of the maximum allowable static friction and the real friction forces.

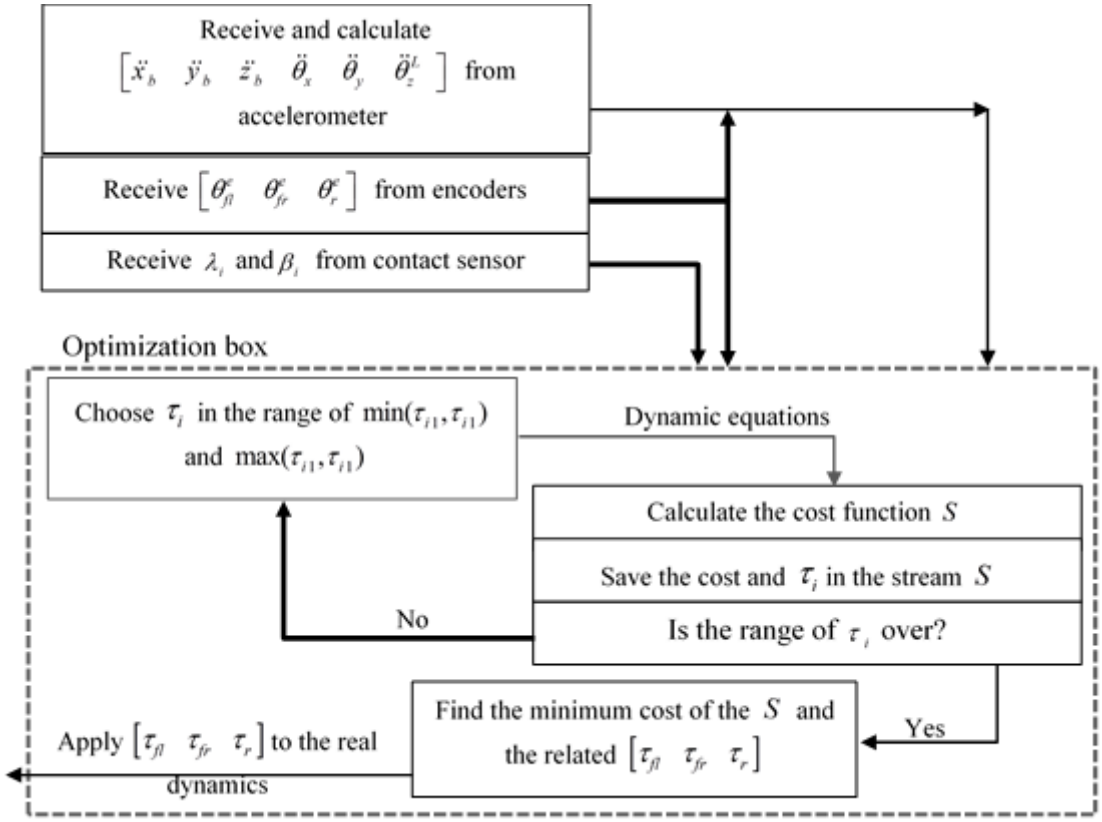

Fig. 6: Optimization flowchart

7 Simulations

The parameters of the UGV utilized for simulation can be numerically defined as $W_b = 0.7$, $L_i^w = 1$, $r_i^\beta = 0.15$, $d_s^o = 0.3$, $x_r^w = 0.1$, $x_f^w = 0$, $H_w^{CG} = 0.2$, $W_s = 0.3$, and $L_t = 2$, where all dimensions are in meter. The masses of the wheel and the main body are equal to 1 (Kg) and 15 (Kg), respectively. The simulation section includes three case studies. In the first case, climbing simulation is conducted to compare an ordinary rover with the proposed extendable platform. Furthermore and the second case shows how the rover overcomes non-symmetric large obstacles when the body rotates about X_{CG}^b which yields different normal contact forces of the front wheels.

7.1 Case study 1: comparison between the rovers during large obstacle climbing

In this case, we first compare the ability of an ordinary rover (Rov1) with the proposed extendable rover (Rov2) during 10 seconds when facing a large obstacle whose surface is defined as

$z = 1.6\pi^{-1}\left(2\text{atan}\left(5\left(x\text{-}4\right)\right)+\pi\right)$. As it can be distinguished from Fig. 7, the ability of the new extendable rover in climbing is significantly improved. The climbing stages of the new rover are shown in Fig. 8. Figure 9-a shows variation of the scissors length. Accordingly, Fig. 9-b shows how the proposed rover successfully adjusts the normal contact forces which yields climbing over obstacle as shown in Figs. 7 and 8.

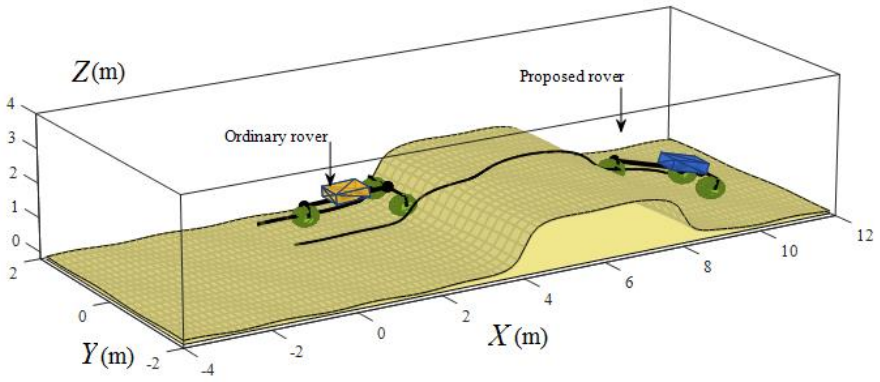

Fig. 7: Obstacle climbing comparison

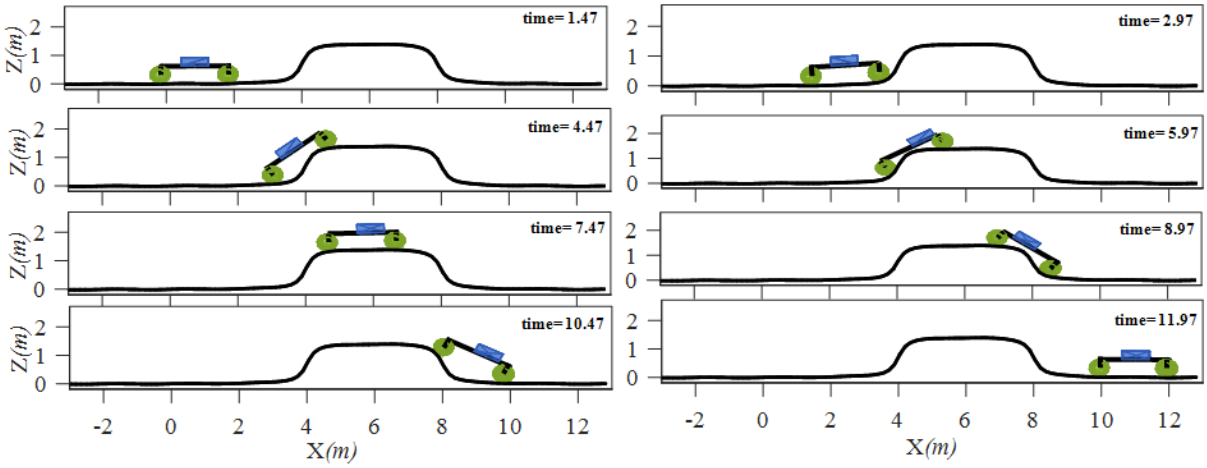

Fig. 8: Sequences of the obstacle climbing

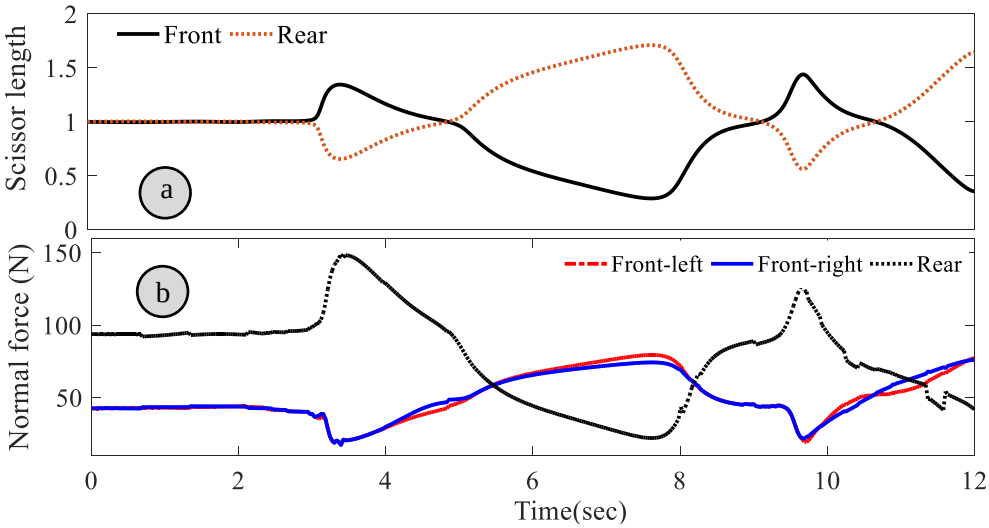

Fig. 9: (a)Variation of the scissors length, (b) Variation of normal contact force

7.2 Case study 2: climbing over a non-symmetric and multi-level obstacle

Symmetric obstacles, which eliminate roll orientation, cause equal contact forces of the front wheels, which is of course unrealistic. This case study investigates the ability of the new extendable rover in climbing over a non-symmetric and multi-level obstacle defined as $z = z_1 z_2$ where

$z_1=\left(\text{atan}(15y)+0.5\pi\right)/\pi+0.7$ and $z_2=0.8\text{atan}(15y)+0.5\pi)/\pi$. Figure 10 shows how the proposed rover successfully climbs the obstacle. According to Fig. 11, it is noticeable that the normal contact forces of the front wheels after *t*=7(s) are different due to the rotation about X_{CG}^{b}.

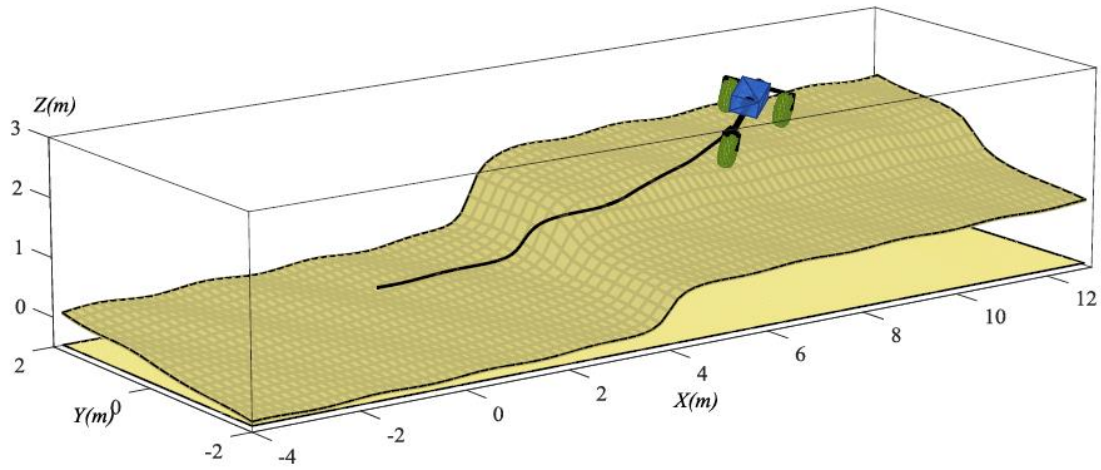

Fig. 10: Climbing over a non-symmetric and multi-level obstacle

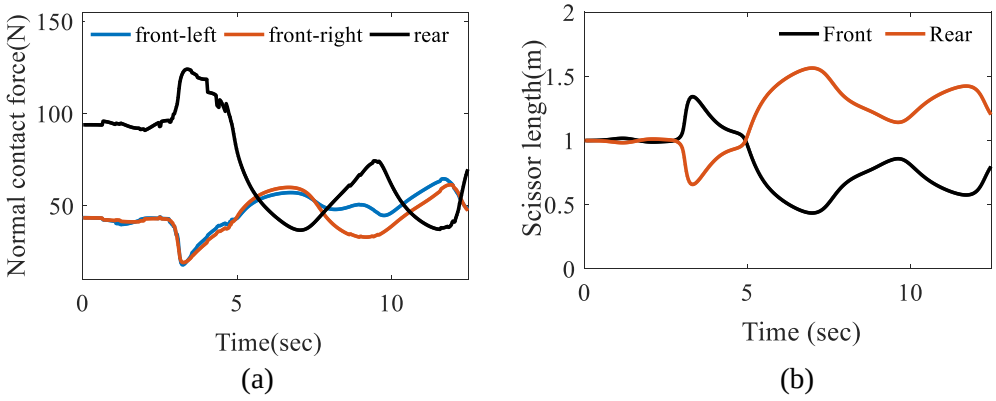

Fig. 11: Normal contact force. (a): normal contact forces, (b): scissors length

Variation of the scissors length during the obstacle climbing is shown in Fig. 11-b which yields proper normal contact forces and successful climbing.

8 Conclusion

This paper proposed a new extendable UGV to challenge the obstacle and cliff. The mass center of the main body was adjusted by implementing a couple of scissor mechanisms which accordingly yielded the normal contact force control and consequently, increased the range of acceptable static friction force. The kinematics and slip-stick Euler-Lagrange dynamics of the rover were formulated when facing the distorted surfaces. The friction cone determine the slip moments. Furthermore, a control process containing scissors length control, geometric position control, and slip reduction algorithm reduced the slip and simultaneously increased the possible tractive force due to the adjustable normal contact forces. This increase in the traction force empowered the extendable rover to overcome large obstacles as compared with the ordinary rovers. On the other hand, the role orientation effect was investigated while climbing over a non-symmetric and multi-level obstacle whose locomotion results showed the successful climbing in the presence of role orientation. The scissors length control process in Section 5 only supported climbing over large obstacles whose height is less than the maximum scissor length. To overcome cliffs and environmental walls, an event-based climbing process was designed which significantly yielded successful climbing over cliffs. Synoptically, according to the climbing results, the new scissor-based platform is efficiently empowered to pass various types of the obstacles which could be impossible for the ordinary rovers.

Reference

[1] A. Zerigui, W. U. Xiang, D. Zong-Quan, "A survey of rover control systems," *International Journal of Computer Sciences and Engineering Systems IJCSES*, vol. 1, no .2, pp. 105-109, 2007.

[2] L. Pedersen, D. Kortenkamp, D. Wettergreen, "A survey of space robotics," 2003.

[3] M. V. Tarasenko, "Transformation of the soviet space program after the cold war," *Science & Global Security*, vol. 4, no .3, pp. 339-361, 1994.

[4] NASA Report," *An Assessment of Balance in NASA's Science Programs*," National Academies Press, 2006.

[5] T. D. J. M. Sanguino, "50 years of rovers for planetary exploration: A retrospective review for future directions," *Robotics and Autonomous Systems*, vol. 94, pp. 172-185, 2017.

[6] H. Li, and C. Schindler, "Investigation of tire-soil interaction with analytical and finite element method," *Mechanics based design of structures and machines*, vol. 41, no.3, pp. 293-315, 2013.

[7] J Guo, H Gao, L Ding, T Guo, Z Deng, "Linear normal stress under a wheel in skid for wheeled mobile robots running on sandy terrain," *Journal of Terramechanics*, vol. 70, pp. 49-57, 2017.

[8] D. A. Homer, A. R. Carrillo, J. F. Peters, & J. E. West, "High resolution soil vehicle interaction modeling," *Journal of Structural Mechanics*, vol. 26, no. 3, pp. 305-318, 1998.

[9] A. Grečenko, "Tire compaction capacity rating on non-standard soil," *Journal of Terramechanics*, vol. 66, pp. 59-61, 2016.

[10] A. Tharakeshwar, A. Ghosal, "Modeling and Simulation of a Three-Wheeled Mobile Robot on Uneven Terrains with Two-Degree-of-Freedom Suspension Mechanisms," *Mechanics Based Design of Structures and Machines*, vol. 43, no. 4, pp. 466-486, 2015.

[11] A. Tharakeshwar, A., A. Ghosal, "A three-wheeled mobile robot for traversing uneven terrain without slip: Simulation and experiments," *Mechanics Based Design of Structures and Machines*, vol. 41, no. 1, pp. 60-78, 2013.

[12] T. Kim, H. S. Kim, J. Kim, "Position-based impedance control for force tracking of a wall-cleaning unit," *International Journal of Precision Engineering and Manufacturing*, vol. 17, no. 3, pp. 323-329, 2016.

[13] K. Naderi, J. Rajamäki, P. Hämäläinen, "Discovering and synthesizing humanoid climbing movements," *ACM Transactions on Graphics (TOG)*, vol. 36, no. 4, pp. 43, 2017.

[14] M. Rashid, et al, "Human fall control system for disabled people using double inverted pendulum," 2017.

[15] A. Siravuru, S. V. Shah, KM Krishna, "An optimal wheel-torque control on a compliant modular robot for wheel-slip minimization," *Robotica*, vol. 35, no. 2, pp. 463-482, 2017.

[16] T. Kobayashi, E Katsuyama, H. Sugiura, et al, "Efficient direct yaw moment control: tyre slip power loss minimisation for four-independent wheel drive vehicle," *Vehicle System Dynamics*, pp. 1-15, 2017.

[17] K. Xu, G. Q. Xu, C. H. Zheng, "Analysis of torque transmitting behavior and wheel slip prevention control during regenerative braking for high speed EMU trains," *Acta Mechanica Sinica* , vol. 32, no .2, pp. 244-251, 2016.

[18] T. Enmei, H. Fujimoto, Y. Hori, D. Gunji, et al, "Slip ratio control using load-side high-resolution encoder for in-wheel-motor with reduction gear," *Mechatronics (ICM) IEEE International Conference on. IEEE*, 2017.

[19] H Gao, C Chen, L Ding, W Li, H Yu, K Xia, Z Liu, "Tracking control of WMRs on loose soil based on mixed H2/H∞ control with longitudinal slip ratio estimation," *Acta Astronautica*, vol. 140, pp. 49-58, 2017.

[20] T. Namba, Y. Yamada, "Fall Risk Reduction for the Elderly Using Mobile Robots Based on the Deep Reinforcement Learning," *Proceeding of the 2017 International Conference on Artificial Life and Robotics (ICAROB 2017)*, 2017.

[21] A. E. LeBouthillier, W. Grey, "walter and his turtle robots", *Robot Build*, vol. 11, no. 5, pp. 1–3, 1999.

[22] T. R. Bridge, "The creep: a fascinating robot vehicle," *Radio Control Models Electron*, pp. 184–186. 1962.

[23] R. Edlinger, M. Zauner, W. Rokitansky, *RoboCup Rescue 2016 Team Description Paper RRT Robocup Rescue 2016 TDP Collection*, pp. 1–8, 2016.

[24] D. Bickler, K. Jewett, H. Eisen, "Mars rover," Patent US D437255 S1, California Institute of Technology, 2001.

[25] J. Jones, J. J. Wu, "inflatable rovers for planetary applications," *Mobile Robots XIV International Society for Optics and Photonics*, vol. 3838, 1999.
[26] B. H. Wilcox, T. Litwin, J. Biesiadecki, et al, "ATHLETE: A cargo handling and manipulation robot for the moon," *Field Robot*, vol. 24, no. 5, pp. 421–434, 2007.
[27] B. Wilcox, "Robotic vehicles for planetary exploration," *Applied Intelligence*, vol. 2, no. 2, pp. 181-193, 1992.
[28] H. Miyamoto, "Current plan of the MELOS, a proposed Japanese Mars mission," *Mars Exploration Program Analysis Groupg Meeting*, 2015.
[29] M Harper, J Pace, N Gupta, C Ordonez, et al, "Kinematic modeling of a RHex-type robot using a neural network," *Unmanned Systems Technology XIX International Society for Optics and Photonics*, vol. 10195, 2017.
[30] A. Mardani, S. Ebrahimi, "Simultaneous surface scanning and stability analysis of wheeled mobile robots using a new spatial sensitive shield sensor," *Robotics and Autonomous Systems*, vol. 98, pp. 1-14, 2017.
[31] A. Mardani, S. Ebrahimi, "A New Resistive Belt Sensor for Multipoint Contact Detection of Robotic Wheels, Accepted for publication in the "*Iranian Journal of Science and Technology, Transactions of Mechanical Engineering*", 2018.